

Cell-Fibronectin Interactions Propel Vertebrate Trunk Elongation via Tissue Mechanics

Nicolas Dray,¹ Andrew Lawton,¹ Amitabha Nandi,¹ Dörthe Jülich,¹ Thierry Emonet,^{1,2} and Scott A. Holley^{1,*}

¹Department of Molecular, Cellular and Developmental Biology

²Department of Physics

Yale University, New Haven, CT 06520, USA

Summary

During embryonic development and tissue homeostasis, cells produce and remodel the extracellular matrix (ECM). The ECM maintains tissue integrity and can serve as a substrate for cell migration. Integrin $\alpha 5$ (*Itg $\alpha 5$*) and αV (*Itg αV*) are the α subunits of the integrins most responsible for both cell adhesion to the ECM protein fibronectin (FN) and FN matrix fibrillogenesis [1, 2]. We perform a systems-level analysis of cell motion in the zebrafish tail bud during trunk elongation in the presence and absence of normal cell-FN interactions. *Itg $\alpha 5$* and *Itg αV* have well-described roles in cell migration in vitro. However, we find that concomitant loss of *itg $\alpha 5$* and *itg αV* leads to a trunk elongation defect without substantive alteration of cell migration. Tissue-specific transgenic rescue experiments suggest that the FN matrix on the surface of the paraxial mesoderm is required for body elongation via its role in defining tissue mechanics and intertissue adhesion.

Results and Discussion

Genetic studies in mouse and zebrafish show that cell-fibronectin (FN) interactions are required for embryonic axis elongation [1–11]. Inhibition of cell-FN interactions via a number of strategies in amphibians produces defects in radial intercalation, mesoderm migration, and gastrulation [12–16]. Imaging of FN and cell dynamics during avian embryogenesis found that the extracellular matrix (ECM) undergoes complex movements that largely mirror the motion of adjacent cells [17–20]. These latter studies suggest that, rather than acting primarily as a substrate for cell migration, the ECM may have a greater mechanical function in force transmission or force generation during morphogenesis [20]. However, given that mechanical stiffening of the *Xenopus* paraxial mesoderm is unaffected by a partial knockdown of FN [21, 22], the underlying requirement(s) for cell-FN interaction in vertebrate body elongation remain unresolved. In zebrafish, *integrin $\alpha 5$* (*itg $\alpha 5$*), *integrin αV* (*itg αV*), and the two *fibronectin* genes are maternally expressed and transcribed in the mesoderm during gastrulation and/or trunk elongation [8–10, 23, 24]. To address the role of cell-FN interactions in vertebrate body elongation, we combined the *itg $\alpha 5$* morpholino or mutant with an *itg αV* morpholino to concomitantly eliminate the function of the two primary FN receptors [8, 25, 26]. We observed a strong body truncation absent in either single mutant or morphant (Figures 1A–1D).

Morphometrics reveal a defect during trunk elongation in *itg $\alpha 5$ ^{mo};itg αV ^{mo}* embryos. At the end of gastrulation, paraxial mesoderm width in *itg $\alpha 5$ ^{mo};itg αV ^{mo}* embryos is normal, indicating that the elongation phenotype is not due to a convergent extension deficiency (Figure S1 available online). However, by the end of trunk elongation, the length of the trunk and tail bud is reduced by 29% (Figure 1). In the zebrafish tail bud, elongation is largely driven by cell migration with a moderate contribution from cell proliferation [27–32]. In *itg $\alpha 5$ ^{mo};itg αV ^{mo}* embryos, we observe a 36% decrease in cell proliferation but observe no substantial change in apoptosis (Figure S1). However, a complete cessation of mitosis throughout gastrulation and body elongation only causes a 22% reduction in trunk and tail length [30]. Thus, the 36% decrease in cell proliferation in *itg $\alpha 5$ ^{mo};itg αV ^{mo}* embryos does not account for the 29% reduction in trunk and tail elongation.

The tail bud is the posterior of the vertebrate embryo consisting of motile progenitors of the vertebrae, skeletal muscle, and spinal cord as well as bipotential neural/mesodermal stem cells [27, 33]. We examined tail bud gene expression patterns to ascertain whether cell fates were affected in *itg $\alpha 5$ ^{mo};itg αV ^{mo}* morphants. We observed no significant change in expression of *tbx6l* ($n = 12$), *eve1* ($n = 14$), or *neurogenin1* ($n = 22$) (Figures 1E–1J). *her1* stripes, representing the segmentation clock, are also present in *itg $\alpha 5$ ^{mo};itg αV ^{mo}* embryos ($n = 59$) (Figures 1K and 1L). These data suggest normal cell differentiation and pattern formation in *itg $\alpha 5$ ^{mo};itg αV ^{mo}* tail buds.

Within the trunk and tail, the FN matrix is primarily found on the paraxial mesoderm surface and somite boundaries (Figure 1M). In *itg $\alpha 5$ ^{mo};itg αV ^{mo}* embryos, FN matrix fibrillogenesis is reduced on the paraxial mesoderm surface, and the fibers have an abnormal anisotropy aligning along the medial-lateral axis (Figure 1N). Segmental FN and all morphological somites are absent.

Given that the FN matrix is a substrate for cell migration, we examined whether the axis truncation in *itg $\alpha 5$ ^{mo};itg αV ^{mo}* embryos is due to aberrant cell movement. We used wild-type (WT) and *itg $\alpha 5$ ^{mo};itg αV ^{mo}* embryos expressing nuclear RFP for three-dimensional (3D) confocal time-lapse imaging, cell tracking, and a systems-level examination of cell motion. After cell tracking, we manually segmented the tail bud into four domains (Figures 2A and 2B and Movie S1) [31]. Within these domains, there are an average of 2,550 cell tracks per time point per embryo. The anterior dorsal medial domain (ADM) is dorsal to the notochord and anterior to the dorsal medial domain (DM). The DM constitutes the posterior of the embryo along with the progenitor zone (PZ), which is ventral to DM and posterior to the notochord. The PZ is characterized by the onset of *tbx6l* and *her1* expression. The presomitic mesoderm (PSM) consists of two bilateral columns of cells flanking the notochord and anterior to the PZ. Cells migrate posteriorly in the ADM and DM, ventrally from the DM into the PZ, and from the PZ to the PSM. Previously, we performed time lapses for an average of 168 min beginning at the eight-somite stage [31]. Here, to extend our analysis of WT cell flow to later trunk elongation, we performed our analysis beginning at the 12-somite stage.

*Correspondence: scott.holley@yale.edu



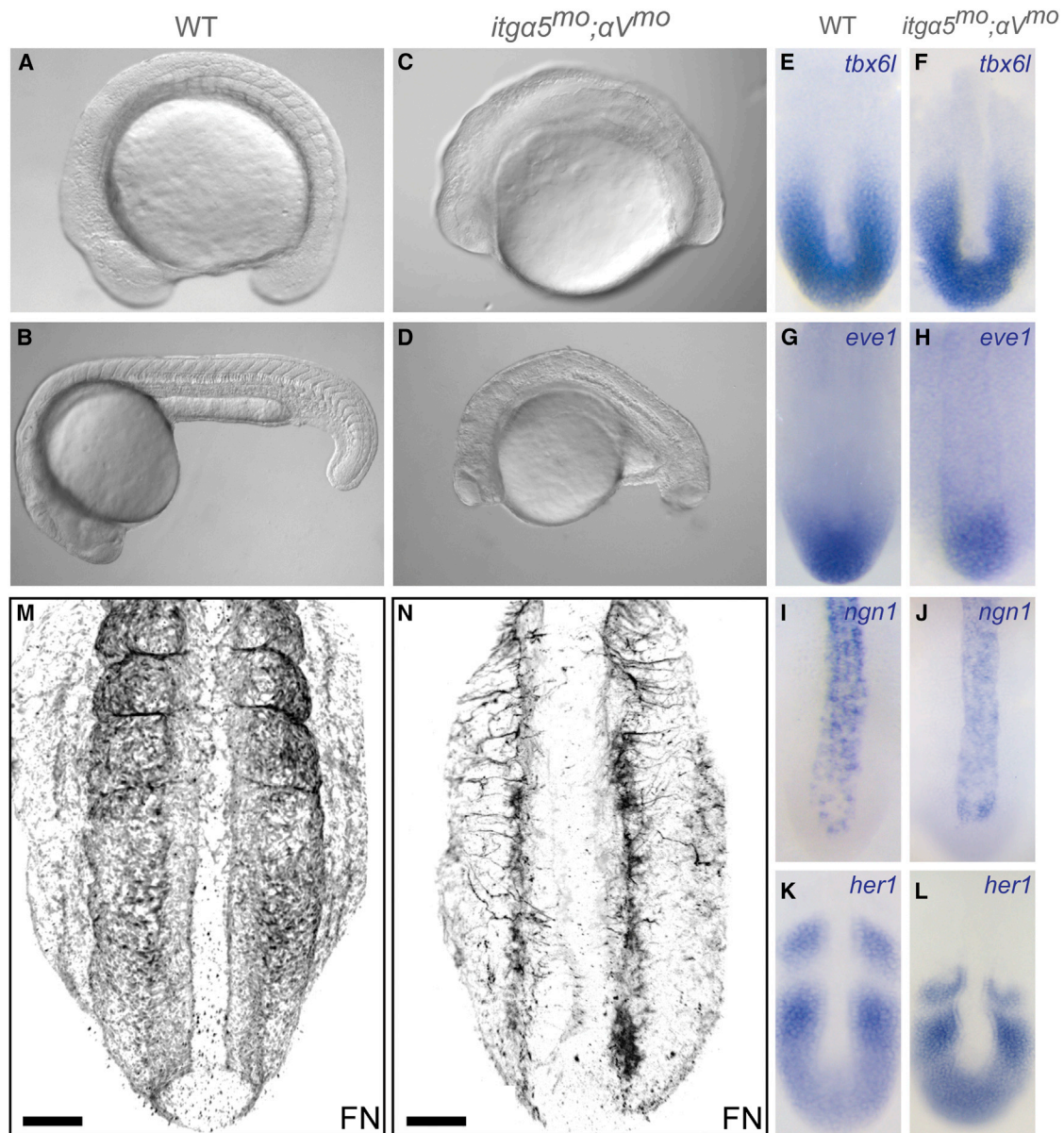


Figure 1. Axis Elongation Defects after Loss of Both *itga5* and *itgaV*

(A–D) Wild-type (WT) (A and B) and truncated (C and D) *itga5^{mo};αV^{mo}* embryos at the end of trunk elongation; i.e., 16-somite-stage embryos (A and C) and 24 hr postfertilization (hpf) (B and D). At the 16-somite stage, we find that distance from the otic vesicle to the anterior of the head in *itga5^{mo};αV^{mo}* embryos (n = 30) is 74% (SD = 8%; p < 0.05) of that in WT embryos (n = 20) and that the distance from the otic vesicle to the tip of the tail is 71% of that in WT embryos (SD = 7%; p < 0.05).

(E–L) In situ hybridization of tail bud gene expression in 13-somite-stage embryos.

(M and N) FN immunolocalization in 16-somite-stage WT (M) (n = 10) and *itga5^{mo};αV^{mo}* embryos (N) (n = 17). Note the reduction in FN matrix as well as the prominent medial-lateral fiber orientation in (N).

Scale bars are 50 μm. In (A–D), anterior is the left. In (E–N), anterior is up. See also Figure S1.

First, cell motion was characterized using raw data to calculate track mean speed, coefficient of variation (C.V., SD divided by the mean), and straightness (Figures 2C, 2E, and 2G). Cell movement within the ADM, DM, and PZ is rapid, shows low C.V., and exhibits the straightest trajectories. Movement in the PSM displays reduced mean speed, higher C.V. of track speed, and lower track straightness relative to the other domains (p < 0.05). These values are consistent with those observed in younger WT embryos except that, in younger embryos, track straightness declines from the DM to PZ while

the C.V. increases [31]. Surprisingly, given their strong axis truncation, *itga5^{mo};αV^{mo}* embryos displayed only two small deviations from WT embryos: increased mean speed and decreased C.V. in the PSM (p < 0.05) (Figures 2D, 2F, and 2H).

We analyzed the spatial pattern of cell flow by calculating average cell motion, segregation of cell flow in the PZ, and local curvature within the cell flow. We projected the 3D cell velocities onto the 2D x- and y-plane in 10 μm² sectors and averaged over the z direction (Figure 2I). Within this vector map, cell motion in each sector was averaged for the entire

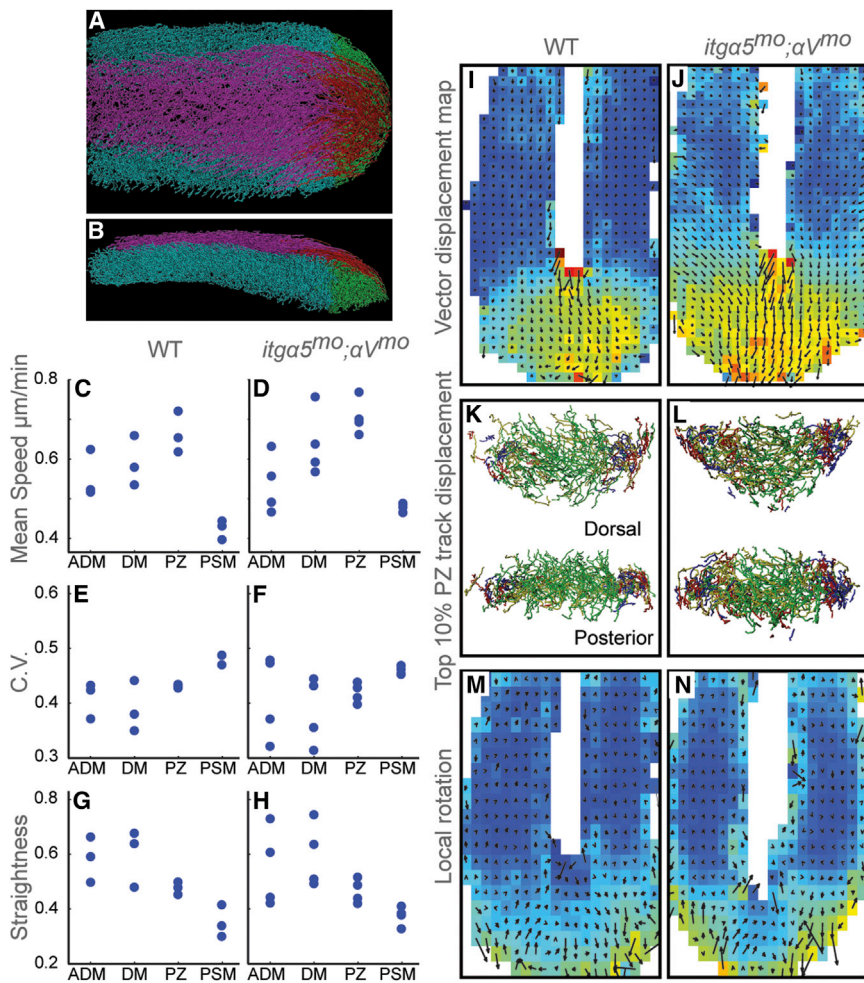


Figure 2. Quantitative Analysis of Cell Motion in the Tail Bud

(A and B) Tail bud cell tracks were divided into four regions: ADM (magenta), DM (red), PZ (green), and PSM (cyan). (A) is a dorsal view and (B) is a lateral view of 12- to 14-somite-stage embryos. Anterior is the left. See also [Movie S1](#). (C and D) Mean track speeds. (E and F) The means of the coefficient of variation (C.V.). (G and H) Track straightness, which is equal to length divided by displacement. (I and J) The vector displacement map averages cell motion in sectors. The heat map indicates mean speed, warmer colors indicate higher speeds, and arrows signify averaged 3D velocity vectors. (K and L) The top 10% of PZ tracks exhibiting the largest displacement in each direction (dorsal to ventral [green], medial to lateral [yellow], posterior to anterior [red], and ventral to dorsal [blue]). (M and N) 3D FEM was used to measure the vorticity within the cell flow. Arrows slanting rightward indicate a dorsal to ventral curvature. The ADM is omitted from the vector map and FEM to better visualize motion in the PSM. In (C–H), data are plotted for three WT and four *itga5^{mo};αV^{mo}* embryos. Data sets averaged 163 min in length. p values were calculated via ANOVA with additional validation by permutation tests. See also [Figure S2](#).

time lapse. Mean speed is indicated by a heat map, and projected velocity is displayed by arrow orientation and length [31]. The vector maps show the rapid cell migration in the posterior tail bud as well as diminished motion in the PSM (Figures 2I and S2). The vectors display the posteriorly directed motion in the DM. The flow pattern in the PZ was revealed via color coding the top 10% of tracks with the largest displacement in each direction (Figures 2K and S2). Here, the ventral migration from the DM into the PZ is highlighted in green, and the medial to lateral flow are highlighted in yellow. The ventral flow is segregated from the dorsal (blue) and anterior (red) migration along the lateral edges of the PZ. Lastly, we calculated the local curvature (i.e., vorticity) of the cell-flow field using the finite element method (FEM) [31]. Vorticity is displayed as a heat map in which warmer colors indicate greater magnitude of the local rotation, and the arrows denote the projection of vorticity vectors. The direction of the arrows is perpendicular to the plane of rotation via the “right-hand rule.” Arrows slanting to the right indicate the dorsal to ventral curvature within the DM and medial PZ (Figures 2M and S2). Again, analysis of the spatial patterns of cell motion in *itga5^{mo};αV^{mo}* embryos revealed no clear change in cell migration (Figures 2J, 2L, 2N, and S2).

Before quantifying cell displacement, global order, and local order within the cell-flow field, we established a reference frame to account for global growth of the embryo and any

shifting of the embryo during the time lapse. Given that the local average velocity of the anterior PSM is relatively low (Figure 2I), we used the anterior 50 μm of the PSM as our reference frame [31]. We calculated the center of mass of the velocities of the anterior 50 μm of the PSM for each time point and subtracted

the movement of this center of mass from all other individual cell velocities for each time point. These relative velocities are used to calculate the mean square displacement (MSD), polarization (Φ), and neighbor similarity of cell motion [31].

We calculated the MSD for each track for the ADM, DM, PZ, and PSM of three WT embryos. A Bayesian analysis of MSD data indicated that the cell motion is best modeled with a diffusion coefficient and velocity magnitude as parameters [34]. The velocity is high and the diffusion coefficient is low in both the ADM and DM (Figures 3A and 3C). Although the velocity does not change as cells migrate from the DM into the PZ, the diffusion coefficient increases ($p < 0.05$). As cells move from the PZ into the PSM, both the velocities and diffusion coefficients decline ($p < 0.05$). This analysis is consistent with our prior model of individual cell motion being self-propelled with the level of noise in determining the direction of migration increasing as a cell migrates into the PZ [31]. We performed a parallel analysis of MSD on four *itga5^{mo};αV^{mo}* embryos, and the only deviation from WT embryos was a small increase in the PZ diffusion coefficient ($p < 0.05$) (Figures 3B and 3D).

Next, we quantified the global and local order of cell motion. To measure the global order within each tail bud zone, we calculated Φ , which varies from 0 (disordered) to 1 (ordered) [35]. In WT embryos, the ADM and DM exhibited high polarization, whereas global order declined as cells

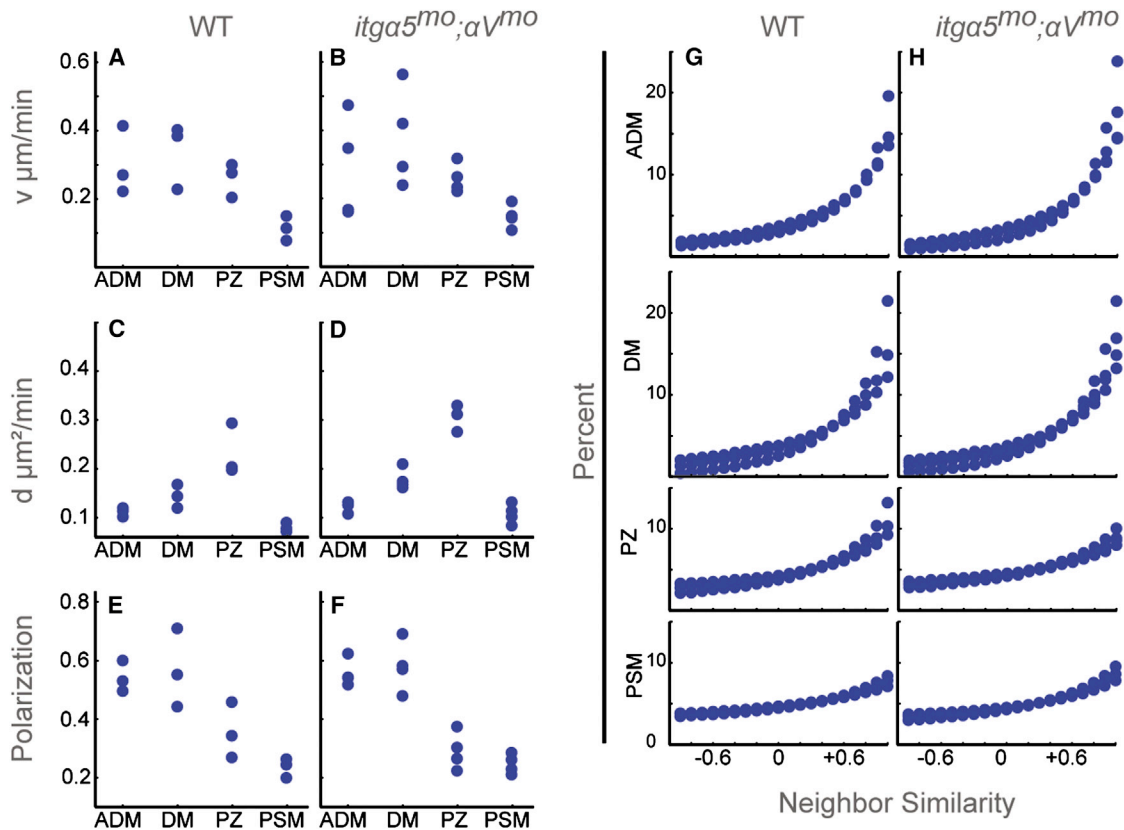


Figure 3. Characterizing Relative Cell Motion: Directed and Diffusive Movement, Global Order, and Local Order

(A–D) A Bayesian analysis of the MSD determined that cell motion in the tail bud is best modeled with velocity magnitude (A and B) and diffusion coefficient (C and D) as parameters [34].

(E and F) Polarization (Φ) measures global order within each domain of the tail bud.

(G and H) Neighbor similarity quantifies the local order of cell motion. The angles between all adjacent instantaneous velocity vectors for each time point are binned such that 1 represents parallel motion, -1 represents antiparallel motion, 0 represents orthogonal motion, and the intervening deciles denote intermediate angles. The percentage of angles in each bin for the three WT and four *itga5^{mo};αV^{mo}* embryos are plotted to give the angle distribution. Overall, there is a switch in the characteristics of the cell motion as cells migrate from the DM to the PZ and from the PZ to the PSM. The pattern of cell motion is maintained in *itga5^{mo};αV^{mo}* embryos.

p values were calculated via paired and unpaired t tests. Data are plotted for three WT embryos and four *itga5^{mo};αV^{mo}* embryos.

migrated from the DM to the PZ ($p < 0.05$) (Figure 3E). The pattern of global order within the tail bud is maintained in *itga5^{mo};αV^{mo}* embryos (Figure 3F). Local order is measured by neighbor similarity, which is the degree to which each cell migrates in the same direction as its immediate neighbors [36]. The ADM and DM cells showed high neighbor similarity, indicating local coherence in cell motion (Figure 3G). By contrast, PZ and PSM cells show less bias in motion relative to neighboring cells. Loss of the FN receptors did not alter neighbor similarity (Figure 3H).

This systematic analysis of cell motion in WT embryos is consistent with our prior study of tail bud cell motion in younger WT embryos [31]. Surprisingly, we find only a few small alterations in cell migration in *itga5^{mo};αV^{mo}* embryos. This result contrasts to the dramatic changes in cell motion that we observed in the zebrafish *cadherin 2* mutant [31]. Altogether, the body elongation phenotype resulting from abrogation of cell-FN interactions does not appear to be due to the alteration of cell migration.

Having discounted aberrant cell migration as an explanation for the *itga5^{mo};αV^{mo}* trunk elongation defect, we sought an alternative hypothesis. The fact that FN fiber anisotropy is

profoundly abnormal in *itga5^{mo};αV^{mo}* embryos (Figure 1N) suggests a misalignment of mechanical forces in the paraxial mesoderm. FN fibrillogenesis is dependent upon actomyosin force transmitted to FN via integrins [37]. In cell culture, mechanical tension is applied to the ECM in the direction of cell motion prior to cell migration [38], and ECM fibers often align along the direction of cell motion [39]. Indeed, FN orientation and convergence extension are governed the same mechanism in *Xenopus* gastrulae [40]. The fiber anisotropy on the paraxial mesoderm of *itga5^{mo};αV^{mo}* embryos is also most likely due to convergent cell migration within the mesoderm and suggests that tension on the surface of the paraxial mesoderm predominantly aligns medial-laterally. This abnormal anisotropy implies that, in WT embryos, a countervailing anterior-posterior tension produces an FN matrix with no bias in fiber alignment. Because we observed no substantive alteration in cell migration in *itga5^{mo};αV^{mo}* embryos, this countervailing tension may instead arise via intra- or intertissue mechanics. At the cellular level, the mechanical changes along the surface of the paraxial mesoderm in *itga5^{mo};αV^{mo}* embryos manifest as ectopic blebbing, which is driven by intracellular hydrostatic pressure (Figures 4A

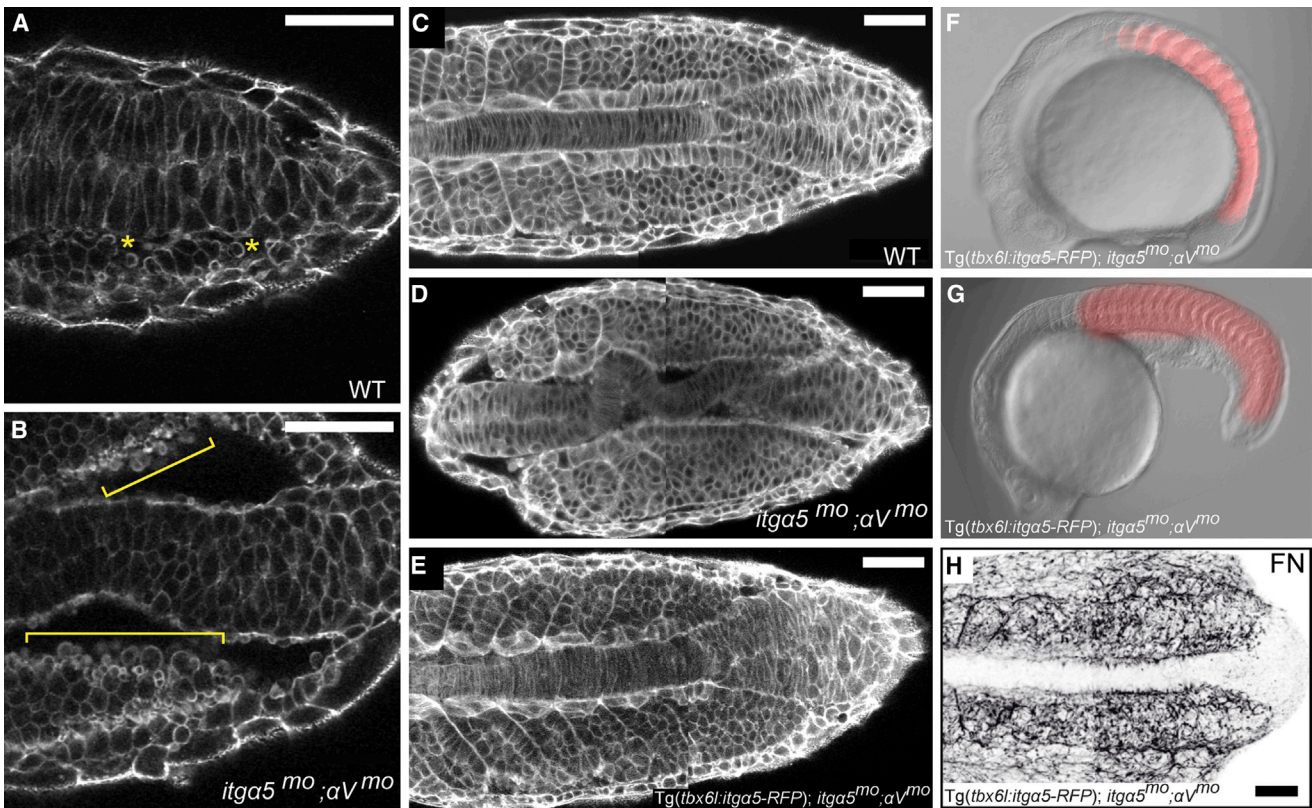


Figure 4. *itgα5* Function in the Paraxial Mesoderm Is Sufficient to Rescue Body Elongation in *itgα5^{mo};αV^{mo}* Embryos

(A) In WT embryos, cells on the surface of the paraxial mesoderm display low levels of blebbing (asterisks), as revealed by phalloidin staining. (B) In *itgα5^{mo};αV^{mo}* embryos, cells along the medial surface of the paraxial mesoderm exhibit a dramatic increase in blebbing (brackets). See also [Movie S2](#). (C–E) Phalloidin staining of the cell cortices shows the close alignment of the notochord and paraxial mesoderm in WT embryos (C) (n = 16), the loss of this intertissue adhesion and alignment in *itgα5^{mo};αV^{mo}* embryos (D) (n = 31), and the rescue of intertissue adhesion and organization in *Tg(tbx6l:itgα5-RFP); itgα5^{mo};αV^{mo}* embryos (E) (n = 10). (F and G) Body elongation is rescued in *Tg(tbx6l:itgα5-RFP);itgα5^{mo};αV^{mo}* embryos at 14 hpf (F) and 24 hpf (G). At the 16-somite stage, the trunks of transgenic rescue embryos (n = 40) are 88% of that in WT embryos (SD = 4%; p < 0.05), and the heads are 83% of that in WT embryos (SD = 5%; p < 0.05). RFP fluorescence shows *Itgα5* expression in the paraxial mesoderm. (H) *Tg(tbx6l:itgα5-RFP)* rescues FN matrix assembly and fiber orientation in *itgα5^{mo};αV^{mo}* embryos (n = 7). Anterior is left. Note that panels (C–E) and (H) are composites of anterior and posterior images. Scale bars represent 50 μm. See also [Figure S3](#).

and 4B and [Movie S2](#)) [41]. The low frequency of blebbing in WT paraxial mesoderm surface cells suggests that the FN matrix constrains both blebbing and the accompanying fluctuations in cytosolic pressure. At the tissue level, the notochord elongates independently of the paraxial mesoderm [42, 43] but, normally, the two tissues are mechanically linked via cell-FN adhesion ([Figure 4C](#)). In *itgα5^{mo};αV^{mo}* embryos, the tissues within the tail bud detach and the notochord undulates as it tries to elongate in the absence of mechanical coupling and concomitant extension of the paraxial mesoderm ([Figure 4D](#)).

We hypothesized that the alteration of cell-FN mechanics in the paraxial mesoderm and/or loss of intertissue adhesion between the notochord and paraxial mesoderm was responsible for the elongation phenotype in *itgα5^{mo};αV^{mo}* embryos. To test this hypothesis, we generated transgenic zebrafish *Tg(tbx6l:itgα5-RFP)* in which *itgα5-RFP* is specifically expressed in the paraxial mesoderm using a *tbx6l* enhancer ([Figures 4F and 4G](#)) [44]. The *itgα5* morpholino is injected to remove endogenous *Itgα5* but will not affect the transgene-lacking sequence complementarity. These transgenics exhibit normal patterns of tail bud gene expression ([Figure S3](#)). Importantly, *Tg(tbx6l:itgα5-RFP) itgα5^{mo};αV^{mo}* embryos have trunks

and tails that are 24% longer than *itgα5^{mo};αV^{mo}* embryos (SD = 14%; p < 0.05) ([Figures 4F and 4G](#)). The transgene rescues assembly of the FN matrix on the paraxial mesoderm ([Figure 4H](#)), adhesion between the paraxial mesoderm and notochord ([Figure 4E](#)), and normal blebbing (data not shown). However, the transgene does not restore cell proliferation ([Figure S1](#)) nor does it rescue the three deviations in cell motion in *itgα5^{mo};αV^{mo}* embryos ([Figure S3](#)).

Our data suggest that a loss of integrin-FN-dependent tissue mechanics and/or intertissue adhesion between the paraxial mesoderm and notochord is the cause of the trunk elongation phenotype in *itgα5^{mo};αV^{mo}* embryos. This conclusion is consistent with both the prescient interpretation of the mouse *fibronectin* knockout phenotype as being due to a defect in tissue assembly and analyses of avian embryos showing that cells and their associated ECM largely form a contiguous entity that is displaced within a continuous flow field [3, 4, 17–20]. Interestingly, in vitro analyses of cell aggregates found that modulating levels of FN and *Itgα5β1* led to tissue phase transitions between a viscoelastic liquid and a viscoelastic solid. The reduction in matrix fibers may reduce apparent tissue viscosity by diminishing global

interconnectivity within the cell aggregates [45]. Altogether, these studies suggest that, rather than the ECM acting primarily as a distinct substrate for cell migration, the cells and ECM exist as an integrated mechanical unit whose fluidity is modulated during tissue morphogenesis.

Experimental Procedures

Zebrafish

Topfel Longfin WT fish and *itg α 5^{tbfe1}* and *itg α 5^{tbfe2}* [8] mutants were maintained according to standard protocols approved by the Institutional Animal Care and Use Committee. Tg(*tbx6l:itg α 5-RFP*) transgenics were generated with the pTol2 β vector plasmid [46]. A 2,510 bp *tbx6l* enhancer [44] PCR fragment was cloned into MCS1 of pTol2 β vector. *itg α 5*-TagRFP (Evrogen) was inserted into MCS2 of pTol2 β vector. Plasmid (164 ng/ μ l) and tol2 transposase messenger RNA (25 ng/ μ l) were coinjected for transgenesis.

In Situ Hybridization and Immunohistochemistry

Immunohistochemistry for FN was performed as previously described [8]. Phalloidin staining with phalloidin-Alexa 488 was performed as previously described [47]. In situ hybridization for *tbx6l*, *her1*, *eve*, and *ngn1* with digoxigenin-labeled antisense probes and NBT/BCIP staining followed standard protocols.

Microinjection, 4D Imaging, and Quantitative Analysis of Cell Motion

itg α 5 morpholino (5'-TAACCGATGTATCAAATCCACTGC-3') [8] and *itg α 5* morpholino (5'-CGGACGAAGTGTTCGCCATGTTT-3') [26] (the underlined sequence overlaps with a morpholino from [25]) were coinjected at 400 μ M and 1,000 μ M, respectively. Time-lapse imaging and cell motion analyses were performed as previously detailed [31] with the addition of the Bayesian MSD analysis [34].

Supplemental Information

Supplemental Information contains three figures and two movies and can be found with this article online at <http://dx.doi.org/10.1016/j.cub.2013.05.052>.

Acknowledgments

We thank N. Monnier for help with the Bayesian MSD analysis; Y. Dufour, H. Zhao, and G. Wagner for statistics advice; and P. McMillen and J. Schwendinger-Schreck for manuscript comments. Funding was provided by National Institutes of Health Developmental Biology training grant T32-HD07180-29 (A.L.), NICHD R01-HD045738, a Research Scholar Grant from the American Cancer Society, NSF IOS-1051839 (S.A.H.), and the Sackler Institute for Biological, Physical and Engineering Sciences (T.E. and S.A.H.).

Received: January 30, 2013

Revised: May 7, 2013

Accepted: May 28, 2013

Published: June 27, 2013

References

1. Takahashi, S., Leiss, M., Moser, M., Ohashi, T., Kitao, T., Heckmann, D., Pfeifer, A., Kessler, H., Takagi, J., Erickson, H.P., and Fässler, R. (2007). The RGD motif in fibronectin is essential for development but dispensable for fibril assembly. *J. Cell Biol.* 178, 167–178.
2. Yang, J.T., Bader, B.L., Kreidberg, J.A., Ullman-Culleré, M., Trevithick, J.E., and Hynes, R.O. (1999). Overlapping and independent functions of fibronectin receptor integrins in early mesodermal development. *Dev. Biol.* 215, 264–277.
3. George, E.L., Georges-Labouesse, E.N., Patel-King, R.S., Rayburn, H., and Hynes, R.O. (1993). Defects in mesoderm, neural tube and vascular development in mouse embryos lacking fibronectin. *Development* 119, 1079–1091.
4. Georges-Labouesse, E.N., George, E.L., Rayburn, H., and Hynes, R.O. (1996). Mesodermal development in mouse embryos mutant for fibronectin. *Dev. Dyn.* 207, 145–156.
5. Goh, K.L., Yang, J.T., and Hynes, R.O. (1997). Mesodermal defects and cranial neural crest apoptosis in alpha5 integrin-null embryos. *Development* 124, 4309–4319.
6. Yang, J.T., Rayburn, H., and Hynes, R.O. (1993). Embryonic mesodermal defects in alpha 5 integrin-deficient mice. *Development* 119, 1093–1105.
7. Girós, A., Grgur, K., Gossler, A., and Costell, M. (2011). α 5 β 1 integrin-mediated adhesion to fibronectin is required for axis elongation and somitogenesis in mice. *PLoS ONE* 6, e22002.
8. Jülich, D., Geisler, R., and Holley, S.A.; Tübingen 2000 Screen Consortium. (2005). Integrinalpha5 and delta/notch signaling have complementary spatiotemporal requirements during zebrafish somitogenesis. *Dev. Cell* 8, 575–586.
9. Koshida, S., Kishimoto, Y., Ustumi, H., Shimizu, T., Furutani-Seiki, M., Kondoh, H., and Takada, S. (2005). Integrinalpha5-dependent fibronectin accumulation for maintenance of somite boundaries in zebrafish embryos. *Dev. Cell* 8, 587–598.
10. Trinh, L.A., and Stainier, D.Y. (2004). Fibronectin regulates epithelial organization during myocardial migration in zebrafish. *Dev. Cell* 6, 371–382.
11. Latimer, A., and Jessen, J.R. (2010). Extracellular matrix assembly and organization during zebrafish gastrulation. *Matrix Biol.* 29, 89–96.
12. Boucaut, J.C., Darribere, T., Li, S.D., Boulekbache, H., Yamada, K.M., and Thiery, J.P. (1985). Evidence for the role of fibronectin in amphibian gastrulation. *J. Embryol. Exp. Morphol. Suppl.* 89, 211–227.
13. Darribère, T., and Schwarzbauer, J.E. (2000). Fibronectin matrix composition and organization can regulate cell migration during amphibian development. *Mech. Dev.* 92, 239–250.
14. Winklbauer, R., and Keller, R.E. (1996). Fibronectin, mesoderm migration, and gastrulation in *Xenopus*. *Dev. Biol.* 177, 413–426.
15. Marsden, M., and DeSimone, D.W. (2001). Regulation of cell polarity, radial intercalation and epiboly in *Xenopus*: novel roles for integrin and fibronectin. *Development* 128, 3635–3647.
16. Rozario, T., Dzamba, B., Weber, G.F., Davidson, L.A., and DeSimone, D.W. (2009). The physical state of fibronectin matrix differentially regulates morphogenetic movements in vivo. *Dev. Biol.* 327, 386–398.
17. Bénazéraf, B., Francois, P., Baker, R.E., Denans, N., Little, C.D., and Pourquié, O. (2010). A random cell motility gradient downstream of FGF controls elongation of an amniote embryo. *Nature* 466, 248–252.
18. Czirik, A., Rongish, B.J., and Little, C.D. (2004). Extracellular matrix dynamics during vertebrate axis formation. *Dev. Biol.* 268, 111–122.
19. Zamir, E.A., Czirik, A., Cui, C., Little, C.D., and Rongish, B.J. (2006). Mesodermal cell displacements during avian gastrulation are due to both individual cell-autonomous and convective tissue movements. *Proc. Natl. Acad. Sci. USA* 103, 19806–19811.
20. Zamir, E.A., Rongish, B.J., and Little, C.D. (2008). The ECM moves during primitive streak formation—computation of ECM versus cellular motion. *PLoS Biol.* 6, e247.
21. Moore, S.W., Keller, R.E., and Koehl, M.A. (1995). The dorsal involuting marginal zone stiffens anisotropically during its convergent extension in the gastrula of *Xenopus laevis*. *Development* 121, 3131–3140.
22. Zhou, J., Kim, H.Y., and Davidson, L.A. (2009). Actomyosin stiffens the vertebrate embryo during crucial stages of elongation and neural tube closure. *Development* 136, 677–688.
23. Ablooglu, A.J., Kang, J., Handin, R.I., Traver, D., and Shattil, S.J. (2007). The zebrafish vitronectin receptor: characterization of integrin alphaV and beta3 expression patterns in early vertebrate development. *Dev. Dyn.* 236, 2268–2276.
24. Crump, J.G., Swartz, M.E., and Kimmel, C.B. (2004). An integrin-dependent role of pouch endoderm in hyoid cartilage development. *PLoS Biol.* 2, E244.
25. Ablooglu, A.J., Tkachenko, E., Kang, J., and Shattil, S.J. (2010). Integrin alphaV is necessary for gastrulation movements that regulate vertebrate body asymmetry. *Development* 137, 3449–3458.
26. Liu, J., Zeng, L., Kennedy, R.M., Gruenig, N.M., and Childs, S.J. (2012). β Pix plays a dual role in cerebral vascular stability and angiogenesis, and interacts with integrin α v β 8. *Dev. Biol.* 363, 95–105.
27. Kanki, J.P., and Ho, R.K. (1997). The development of the posterior body in zebrafish. *Development* 124, 881–893.
28. Harrington, M.J., Chalasani, K., and Brewster, R. (2010). Cellular mechanisms of posterior neural tube morphogenesis in the zebrafish. *Dev. Dyn.* 239, 747–762.

29. Quesada-Hernández, E., Caneparo, L., Schneider, S., Winkler, S., Liebling, M., Fraser, S.E., and Heisenberg, C.P. (2010). Stereotypical cell division orientation controls neural rod midline formation in zebrafish. *Curr. Biol.* *20*, 1966–1972.
30. Zhang, L., Kendrick, C., Jülich, D., and Holley, S.A. (2008). Cell cycle progression is required for zebrafish somite morphogenesis but not segmentation clock function. *Development* *135*, 2065–2070.
31. Lawton, A.K., Nandi, A., Stulberg, M.J., Dray, N., Sneddon, M.W., Pontius, W., Emonet, T., and Holley, S.A. (2013). Regulated tissue fluidity steers zebrafish body elongation. *Development* *140*, 573–582.
32. Fior, R., Maxwell, A.A., Ma, T.P., Vezaro, A., Moens, C.B., Amacher, S.L., Lewis, J., and Saúde, L. (2012). The differentiation and movement of presomitic mesoderm progenitor cells are controlled by Mesogenin 1. *Development* *139*, 4656–4665.
33. Martin, B.L., and Kimelman, D. (2012). Canonical Wnt signaling dynamically controls multiple stem cell fate decisions during vertebrate body formation. *Dev. Cell* *22*, 223–232.
34. Monnier, N., Guo, S.M., Mori, M., He, J., Lénárt, P., and Bathe, M. (2012). Bayesian approach to MSD-based analysis of particle motion in live cells. *Biophys. J.* *103*, 616–626.
35. Cavagna, A., Cimarelli, A., Giardina, I., Parisi, G., Santagati, R., Stefanini, F., and Viale, M. (2010). Scale-free correlations in starling flocks. *Proc. Natl. Acad. Sci. USA* *107*, 11865–11870.
36. Arboleda-Estudillo, Y., Krieg, M., Stühmer, J., Licata, N.A., Muller, D.J., and Heisenberg, C.P. (2010). Movement directionality in collective migration of germ layer progenitors. *Curr. Biol.* *20*, 161–169.
37. Schwarzbauer, J.E., and DeSimone, D.W. (2011). Fibronectins, their fibrillogenesis, and in vivo functions. *Cold Spring Harb. Perspect. Biol.* *3*, 3.
38. Trepap, X., Wasserman, M.R., Angelini, T.E., Millet, E., Weitz, D.A., Butler, J.P., and Fredberg, J.J. (2009). Physical forces during collective cell migration. *Nat. Phys.* *5*, 426–430.
39. Czirok, A., Zach, J., Kozel, B.A., Mecham, R.P., Davis, E.C., and Rongish, B.J. (2006). Elastic fiber macro-assembly is a hierarchical, cell motion-mediated process. *J. Cell. Physiol.* *207*, 97–106.
40. Goto, T., Davidson, L., Asashima, M., and Keller, R. (2005). Planar cell polarity genes regulate polarized extracellular matrix deposition during frog gastrulation. *Curr. Biol.* *15*, 787–793.
41. Charras, G., and Paluch, E. (2008). Blebs lead the way: how to migrate without lamellipodia. *Nat. Rev. Mol. Cell Biol.* *9*, 730–736.
42. Ellis, K., Bagwell, J., and Bagnat, M. (2013). Notochord vacuoles are lysosome-related organelles that function in axis and spine morphogenesis. *J. Cell Biol.* *200*, 667–679.
43. Stemple, D.L. (2005). Structure and function of the notochord: an essential organ for chordate development. *Development* *132*, 2503–2512.
44. Szeto, D.P., and Kimelman, D. (2004). Combinatorial gene regulation by Bmp and Wnt in zebrafish posterior mesoderm formation. *Development* *131*, 3751–3760.
45. Caicedo-Carvajal, C.E., Shinbrot, T., and Foty, R.A. (2010). Alpha5beta1 integrin-fibronectin interactions specify liquid to solid phase transition of 3D cellular aggregates. *PLoS ONE* *5*, e11830.
46. Brend, T., and Holley, S.A. (2009). Expression of the oscillating gene *her1* is directly regulated by Hairy/Enhancer of Split, T-box, and Suppressor of Hairless proteins in the zebrafish segmentation clock. *Dev. Dyn.* *238*, 2745–2759.
47. Jülich, D., Mould, A.P., Koper, E., and Holley, S.A. (2009). Control of extracellular matrix assembly along tissue boundaries via Integrin and Eph/Ephrin signaling. *Development* *136*, 2913–2921.